Comparative assessment of PIV-based pressure evaluation techniques applied to a transonic base flow

Paul Blinde[1*], Dirk Michaelis[2], Bas van Oudheusden[1], Pierre-Elie Weiss[3], Roeland de Kat[4], Angeliki Laskari[4], Young Jin Jeon[5], Laurent David[5], Daniel Schanz[6], Florian Huhn[6], Sebastian Gesemann[6], Matteo Novara[6], Cameron McPhaden[7], Nathan Neeteson[7], David Rival[7], Jan FG Schneiders[1], Ferry Schrijer[1]

1: Faculty of Aerospace Engineering, Delft University of Technology, The Netherlands
2: LaVision GmbH, Göttingen, Germany
3: ONERA, The French Aerospace Lab, F-92190 Meudon, France
4: Engineering and the Environment, University of Southhampton, Southampton, UK
5: Institut PPRIME, UPR3346, CNRS – Université de Poitiers – ISAE-ENSMA, France
6: Dept. of Experimental Methods, Institute of Aerodynamics and Flow Technology, German Aerospace Center (DLR), Göttingen, Germany
7: Dept. of Mechanical and Materials Engineering, Queen's University, Kingston, Canada
* corresponding author: p.l.blinde@tudelft.nl

Keywords: tomographic PIV, particle tracking, pressure determination

ABSTRACT

A test case for PIV-based pressure evaluation techniques has been developed by constructing a simulated experiment from a ZDES simulation for an axisymmetric base flow at Mach 0.7. The test case comprises sequences of four subsequent particle images (representing multi-pulse data) as well as continuous time-resolved data. Particle images were processed using tomographic PIV processing as well as the PTV algorithm 'Shake-The-Box'. Multiple pressure reconstruction techniques have subsequently been applied to the PIV results (Eulerian approach, iterative least-square pseudo-tracking, Taylor's hypothesis approach, instantaneous Vortex-in-Cell) and PTV results (FlowFit, Vortex-in-Cell-plus, Voronoi-based pressure evaluation and iterative least-square pseudo-tracking). All methods were able to reconstruct the main features of the instantaneous pressure fields, including methods that reconstruct pressure from a single PIV velocity snapshot. Highly accurate pressure field reconstructions could be obtained by using PTV approaches in combination with more advanced techniques. In general, the use of longer series of time-resolved input data, when available, allows more accurate pressure field reconstruction. Noise in the input data typically reduces the accuracy of the reconstructed pressure fields, but none of the techniques proved to be critically sensitive to the amount of noise added in the present test case.

1. Introduction

Fluid pressure is directly relevant to phenomena like surface loading and sound generation (aeroacoustics) and as such an important quantity in many engineering problems. The quantification of mean and fluctuating pressure is therefore of relevance for efficient designs. While surface pressure can experimentally be determined with pressure transducers and pressure-sensitive paint (PSP), the novel approach of PIV-based pressure determination (van Oudheusden 2013) offers unique new capabilities. Compared to the more established

measurement techniques, PIV-based pressure determination does not require instrumentation or surface preparation of the wind tunnel model. This allows for pressure determination in configurations where such modifications are not practical, e.g. very thin (or membrane-like) airfoils. In more regular configurations, it avoids the installation of large numbers of pressure transducers which is a common practice to obtain reliable surface load distributions. Another unique feature of PIV-based pressure determination is its inherent ability to provide simultaneous velocity and pressure data in the full flow field, which enables a better insight in the relation between fluid dynamics and surface loads or sound fields.

Given these beneficial features, there has been a long and increasing interest in PIV-based pressure determination. In recent years, moreover, the technique has become increasingly feasible and appealing, especially due to the development of (time-resolved) volumetric diagnostic capabilities, such as tomographic PIV (Elsinga et al. 2006; Scarano 2013) and Lagrangian particle tracking (Schanz et al. 2016). Many studies have addressed different implementations of this technique (van Oudheusden 2013). With the maturing of the method, its scale-up from small-size research environments is currently receiving attention in collaborative European framework programs like 'AFDAR' and 'NIOPLEX'. The particular work described in the current paper reflects a joint effort by partners in 'NIOPLEX', and to the authors' knowledge establishes the first systematic comparative study, in which multiple groups are involved that work on the same test case for pressure determination (similar as in the "PIV challenges").

2. Basic working principle

In PIV-based pressure determination, velocity data obtained with PIV is used to compute the local pressure gradient (∇p) from the momentum equation (equation 1), with pressure being subsequently obtained through spatial integration.

$$\nabla p = -\rho \frac{D\mathbf{u}}{Dt} \tag{1}$$

Here ρ is the density and $D\mathbf{u}/Dt$ is the material acceleration, which is the acceleration of a fluid particle in a Lagrangian perspective, and which is obtained from the flow field measurement. For incompressible flow the density is a constant, while under compressible flow conditions, the density can be eliminated as independent variable by combining the momentum and energy equations (van Oudheusden et al. 2007). Also note that by time-averaging of equation 1, mean

pressure fields can be obtained from uncorrelated velocity fields (e.g. van Oudheusden et al. 2007).

The experimental determination of the material acceleration from PIV measurements has been subject of extensive research, for which different methods have been proposed. Using two or more velocity fields closely separated in time, the material acceleration can be determined via a Lagrangian formulation by tracing imaginary fluid particles over subsequent velocity fields (e.g. Liu and Katz 2006) or via an Eulerian formulation by separately determining local temporal and spatial velocity derivatives from the structured velocity measurement grid (e.g. Baur and Köngeter 1999). To alleviate the need for time-resolved velocity data, methods have been proposed to calculate the material acceleration from velocity data at a single time instance by employing physical models (e.g. de Kat and Ganapathisubramani 2013; Laskari et al. 2016; Schneiders et al. 2016). Alternative to taking velocity fields as a starting point, the material acceleration can also be obtained from the recorded particle images, by tracing individual particles (PTV) or particle patterns (e.g. FTEE, Jeon et al. 2014). The PTV-based strategy includes conventional tracking approaches that rely on relatively low particle seeding concentrations (e.g. Malik et al. 1993) as well as more recently proposed advanced approaches that avoid this drawback (e.g. Novara and Scarano 2013; Schanz et al. 2016). Also for the integration of the pressure gradient, different procedures have been suggested and tested, such as direct spatial integration (e.g. Baur and Köngeter 1999, Tronchin et al. 2015) and Poisson formulations (e.g., de Kat and van Oudheusden 2012).

Depending on the followed approach, the performance of different PIV-based pressure evaluation techniques is influenced by the characteristics of the flow as well as the quality of the measurement data. The relative strengths, weaknesses and dependencies of different approaches have been addressed in the past in a number of comparative performance assessments (see van Oudheusden (2013) for a review). The present study contributes to these efforts by making a controlled assessment, through the application of a wide variety of state-of-the-art velocimetry-based pressure determination techniques (see Table 1) to the same test case and employing the same underlying synthetic particle-image data. The techniques are classified in PIV-based techniques (1 to 4), which rely on the velocity data obtained with cross-correlation of particle images/ volumes between two time instances, and PTV-based techniques (4 to 8), that require tracking of individual particles. A further distinction is made between techniques that work with data at a single time-instance only (3 and 4) and techniques that require time-resolved input data (all others).

Table. 1 Overview of pressure evaluation techniques considered in this study.

No.	Abbrev.	Velocity measurement	Determination of material acceleration	Integration of pressure gradient
1	EUL	PIV	Eulerian approach	Poisson solver
4	ILAG	PIV	Iterative least-square pseudo-tracking	Poisson solver
2	TH	PIV	Taylor's hypothesis approach	Poisson solver
3	IVIC	PIV	Instantaneous Vortex-in-Cell	Poisson solver
5	FF1	PTV ('Shake-The-Box') + FlowFit		FFT
6	FF2	PTV ('Shake-The-Box')		FlowFit2
7	VIC+	PTV ('Shake-The-Box') + Vortex-in-Cell-plus		Poisson solver
8	VOR	PTV ('Shake-The-Box')		Voronoi-based integration

3. Description of the test case

The test case consists of the transonic flow over an axisymmetric step, which forms a simplified representation of the flow over the base of a launcher during its ascent phase. The flow over the launcher base gives rise to fluctuating side loads on the nozzle and quantifying these loads is critical for the efficient design of nozzles and surrounding structures. Apart from this industrial relevance, the choice for the test case is further motivated by its richness in terms of spatial and temporal flow scales and its challenging nature that is inherent to high-speed three-dimensional separating-reattaching flows. It should be remarked here that not all applied techniques perform optimal for the flow conditions under consideration and this test case alone therefore does not constitute an exhaustive performance assessment of the different methods. These limitations should be kept in mind when interpreting the results of the study.

To have reference data available against which the pressure results can be validated, the test case is based on a numerical simulation. A PIV experiment is simulated by creating synthetic particle images of a virtual measurement volume. Model geometry (see Figure 3) and flow conditions are designed to represent typical experimental arrangements in the 27×27 cm^2 transonic-supersonic wind tunnel at the Aerodynamics Laboratory at Delft University of Technology. The model main body has a diameter (D) of 50 mm and has an afterbody of diameter (d) of 20 mm (0.4D), resulting in a step height of 15 mm (0.3D). Wind tunnel walls are omitted in the simulation for simplicity and robustness. The free stream flow has a Mach number (M_∞) of 0.7, total pressure (p_t) of 200 kPa and total temperature (T_t) of 285 K. Using the isentropic flow relations, this corresponds to a free stream pressure of 144,186 Pa, a free stream temperature of 260 K, and a free stream velocity (U_∞) of 226 m.s^{-1}. The Reynolds number based on the model main body

diameter (Re_D) is 1.3 million. The measurement domain of the simulated PIV experiment has a size of 1.2D × 0.47D × 0.08D (60 mm × 24 mm × 4 mm, L × H × W).

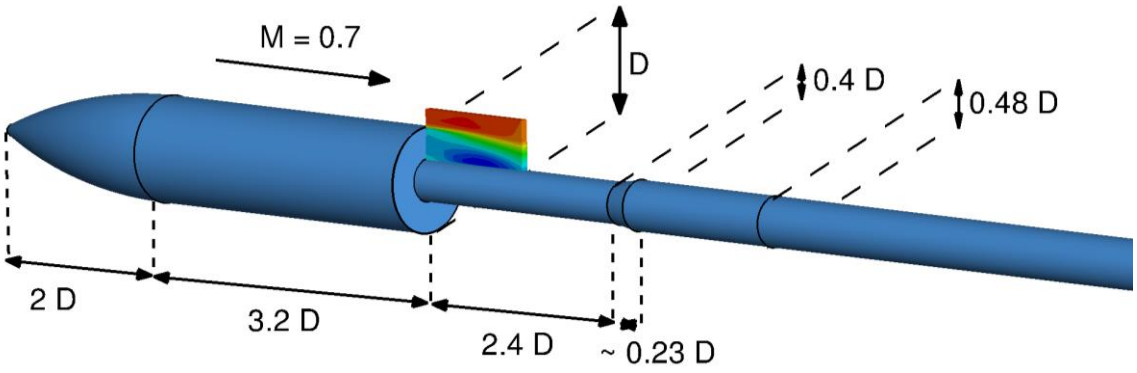

Fig. 1 Sketch of the geometry; Diameter D equals 50 mm. Filled coloured contours depict the mean streamwise velocity in the virtual measurement volume for the simulated PIV experiment.

Synthetic particle images are processed using tomographic PIV algorithms (Elsinga et al. 2006) as well as with the PTV algorithm 'Shake-The-Box' (STB, Schanz et al. 2016). This enables the use of PIV-based pressure determination techniques that require velocity input data on a Cartesian grid, as well as PTV-based techniques which take scattered data available at particle positions as starting point. To be able to assess the impact of measurement noise, processing is performed using both idealized, noise-free particle images ('clean') as well as particle images to which a controlled amount of artificial noise is added ('noisy').

The test case comprises sequences of four subsequent images as well as continuous time-resolved data. This distinction is motived by considerations with respect to the limitations encountered under actual measurement conditions. The multi-pulse data can actually be made available for high-speed flows by using PIV systems with multiple independent laser and camera systems (e.g. Souverein et al. 2009; Lynch and Scarano 2014a). Continuous series of time-resolved data on the other hand cannot realistically be obtained for the present flow case (i.e. a high-speed transonic flow) within the limits of current measurement capabilities. For low-speed flows, modern high-speed laser and camera equipment do however allow sufficiently high sample rates to perform time-resolved PIV measurements. It is therefore deemed insightful to consider the time-resolved datasets as a means to assess pressure extraction capabilities for (low-speed) flow conditions.

Figure 2 shows the organisation of the extracted datasets with the numbering of the velocity snapshots and images as well as the associated time separation. Note that the smaller time separation of 2 µs is equal to the time separation for PIV processing. The larger time separation of 10 µs used in the multi-pulse data was found to be suitable as time separation for determining the material acceleration based on a preliminary assessment by Blinde et al. (2014).

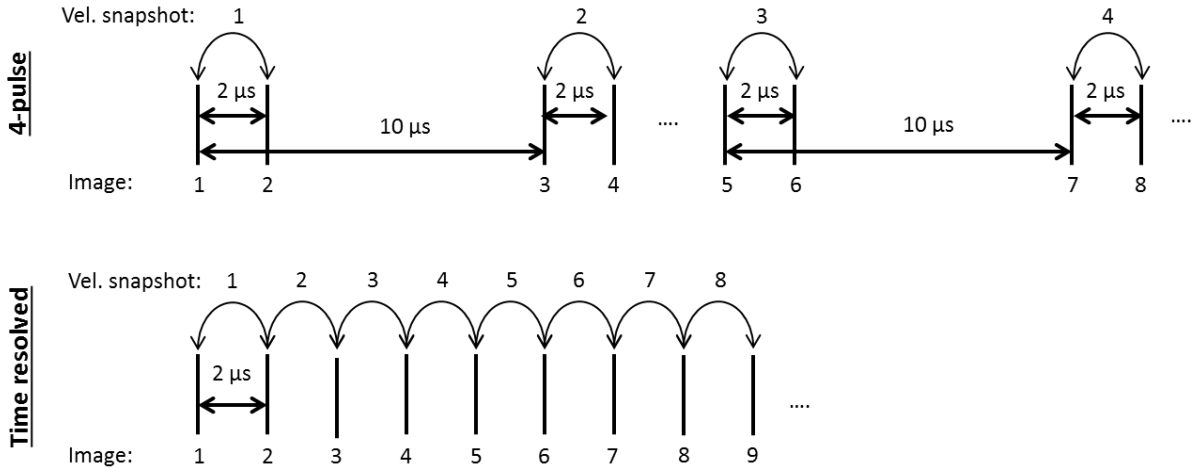

Fig. 2 Time-separation diagrams for consecutive particle images, 4-pulse data (top) and continuous time-resolved data sets (bottom)

Table 2 provides an overview of the resulting datasets. In an experimental investigation, the measurement provides velocity field data, but the true value of the pressure is not available to the researcher. To mimic this situation, the reference pressure data from the numerical simulation were kept isolated from the researchers that applied the pressure determination techniques.

Table. 2 Overview of datasets. 'Clean' and 'Noisy' refer to the cases without or with artificial noise added to the particle images. The 'clean' and 'noisy' cases consider different time instances, so that the exact noise levels cannot be obtained by comparing the two cases.

Type	**Description**
Continuous time-resolved data ('clean' and 'noisy')	- Particles images at 42 consecutive time instances - 41 velocity snapshots obtained through PIV processing. - Velocity and acceleration data at particle positions at same 21 time instance as PIV velocity fields, obtained through STB processing.
4-pulse data ('clean' and 'noisy')	- 21 sets of particle images at 4 consecutive time instances - 21 sets of 2 consecutive velocity snapshots obtained through PIV processing - Velocity and acceleration data at particle positions at the middle time instances of the sets of particle images/ velocities, obtained through STB processing.

Table. 2 Overview of datasets (continued)

Type	Description
Velocity statistics	- Mean and r.m.s. velocity fields based on full dataset (5000 snapshots) obtained through PIV processing of 'clean' particle images
Camera calibration	- Calibration images for four virtual cameras
Reference PIV	- Velocity, density and pressure data from the numerical simulation interpolated to the PIV grid positions
Reference STB	- Velocity, density and pressure data from the numerical simulation interpolated to the particle positions

4. Details of simulated experiment

4.1 Zonal detached eddy simulation (ZDES)

A dedicated ZDES simulation (Deck 2005, 2012) is performed building on ample experience with applying ZDES to axisymmetric base flows (e.g. Deck and Thorigny 2007; Weiss et al. 2009; Weiss and Deck 2011). ZDES is closely related to the classical detached eddy simulation. The main difference between the two approaches is that within ZDES the user has to select the RANS and DES domains. The selection of the appropriate mode depends on the nature of the flow problem. Given that the flow separation is fixed by the geometry, a mode I (i.e. DES) has been retained for the separated area and a mode 0 (i.e. URANS) upstream from the separation occurring at the trailing edge of the forebody.

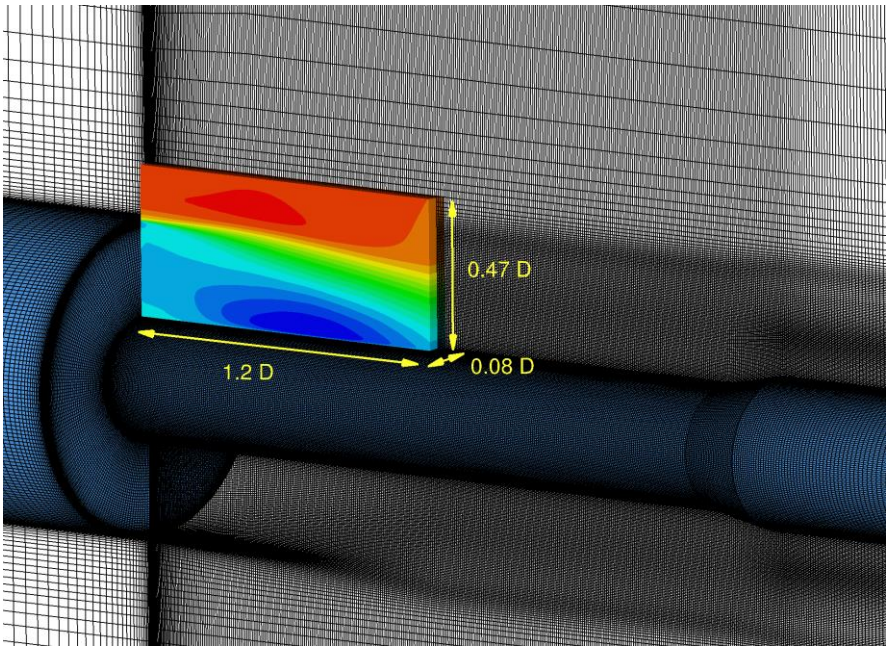

Fig. 3 Detail of mesh with sketch of the geometry; Filled coloured contours depict the mean streamwise velocity in the virtual measurement volume for the simulated PIV experiment.

Model geometry and flow conditions have been presented in section 3. The simulation uses a cylindrical grid with 17 million points of which 10 million points are located in the separated area. The virtual PIV volume contains close to 300,000 points (see Figure 3). The grid is locally refined at the location of the shear layer. Calculations are performed with a time step (Δt_{ZDES}) of 0.5 µs. 5000 snapshots are sampled with a time separation 2 µs ($\Delta t_{sampling}$), covering a total time duration of 10 ms. According to the Nyquist–Shannon criterion, this sampling allows to resolve temporal scales with Strouhal numbers (St_D) from 0.02 to 55. This high temporal resolution was adopted to increase the accuracy for the calculation of particle tracks. The output data used for this study consist of velocity, density and pressure values.

Figure 4 shows the mean streamwise velocity, mean pressure as well as the turbulence intensity and the root mean square (r.m.s) of the pressure fluctuations in a radial plane of the simulated domain. Here, the pressure coefficient (C_p) and the turbulence intensity (T.I.) are defined as:

$$C_p = \frac{\frac{p}{p_\infty} - 1}{\frac{1}{2}\gamma M_\infty^2} \qquad (2)$$

$$T.I. = \sqrt{\frac{1}{3}((u'_{RMS})^2 + (v'_{RMS})^2 + (w'_{RMS})^2)}\,/U_\infty \qquad (3)$$

In these equations γ denotes the ratio of specific heats, and u'_{RMS}, v'_{RMS} and w'_{RMS} denote the r.m.s. of the fluctuating velocity components in x-, y- and z-direction, respectively. Results have been obtained on the basis of 5000 time samples and considering all planes in azimuthal direction to improve the statistical convergence. The bottom left figure shows the location of the measurement volume for the simulated PIV experiment (see dashed box).

The mean flow field (top left figure) shows a shear layer that emanates from the corner of the step at y/ D = 0.3 and grows in downstream direction. The mean reattachment of the shear layer occurs at approximately x/ D = 1.25, which is just outside the virtual PIV measurement volume. Below the shear layer, a recirculation region occurs, where the mean velocity reaches a minimum of -0.30U_∞, while the minimum mean pressure ($C_{p,min}$) is -0.23. Downstream of the point of mean reattachment, a high pressure region occurs, where the maximum mean pressure ($C_{p,max}$) of 0.18 is attained at x/ D = 1.50. The figures on the right show elevated levels of turbulence intensity and pressure fluctuations in the shear layer and the reattachment region, with maxima of $T.I._{max}$ = 0.30 and $Cp'_{RMS,max}$ = 0.08 located at about x/ D = 1.0D; y/ D= 0.2D.

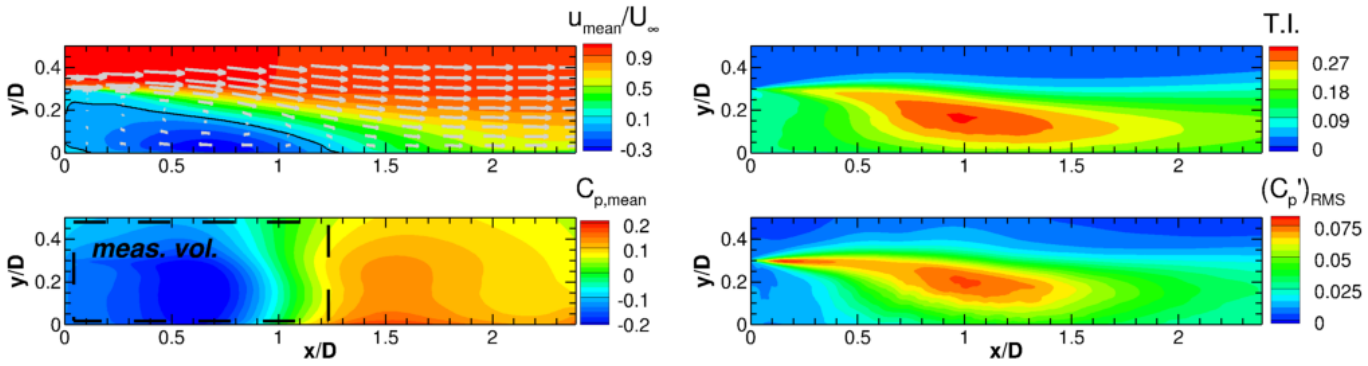

Figure 4. Mean streamwise velocity (top-left), mean pressure (bottom-left), turbulence intensity (top right) and root mean square of normalised pressure fluctuations (bottom-right); Top left figure: black solid line indicates zero mean streamwise velocity; vectors have been subsampled for clarity; Bottom-left figure: dashed box indicates the measurement volume of the simulated PIV experiment.

Figure 5 depicts a representative realisation of the instantaneous streamwise velocity, density, pressure and streamwise material acceleration. Especially the material acceleration field (bottom right) shows small-scale flow structures originating from the corner of the step that break down towards the reattachment region which is characterised by the presence of interacting flow structures with a variety of length scales.

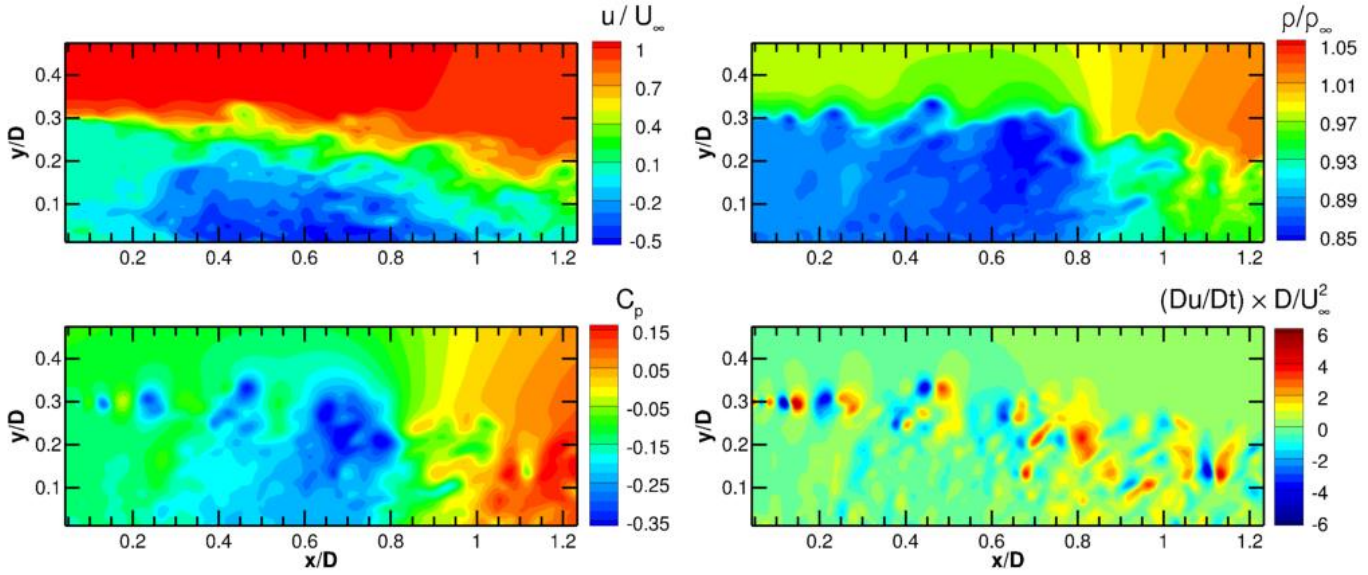

Figure 5. Instantaneous velocity (top left), density (top right), pressure (bottom left) and streamwise material acceleration (bottom right)

4.2 Calculation of particle tracks

The PIV measurement domain is randomly seeded with particles so that the synthetic PIV images contain 0.05 particles per pixel (ppp). The particles are propagated using an explicit, fourth-order Runge-Kutta method in combination with spline interpolation in time and natural neighbour interpolation in space. Three time integration steps are performed per simulation sampling time step of 2 μs, so that the Courant number is smaller than 1 and the Courant–Friedrichs–Lewy (CFL) condition is met in the full domain with the exception of a thin region in the direct vicinity of the corner of the step. To allow inflow of new particles, a narrow region surrounding the measurement volume is randomly seeded with particles after each time step.

The instantaneous particle velocity is taken equal to the instantaneous fluid velocity at the particle position, which is a valid approach for the great majority of the flow field, where the flow timescales are smaller than the typical seeding particle relaxation time (τ_p) of approximately 2 μs (Ragni et al. 2010). To assess the numerical errors from integration and interpolation, particles are integrated one sample time step forward and subsequently backward in time. Comparing the resulting position with the original position yields a local error estimate of below 10^{-5} U_∞, (< 0.0001 voxel displacement). In a second test, targeted at quantifying the errors due to interpolation, particle positions are integrated one sample time step forward in time using the original simulation data and the simulation data subsampled at half the spatial and temporal resolution. Comparing the resulting positions and assuming that the error scales with 2^4 of the spatial and temporal resolution (valid for 4th-order methods), yields typical local r.m.s. error estimates of $<0.003U_\infty$ (<0.03 voxel displacement).

4.3 Generation of synthetic particle images

The settings used for generating the synthetic images are chosen to represent typical PIV measurements of a transonic flow. Particle images are recorded every 2 μs by four virtual cameras with a chip size of 1624 × 800 pixels and a pixel pitch of 4.4 μm. The three-dimensional particle positions are projected onto the two-dimensional sensors via a pinhole camera model. The four cameras are placed in a cross configuration with yaw and pitch angles of +/ - 30° to correspond to a total system aperture of 60°, an optimal configuration for tomographic reconstruction (Scarano 2013). They are equipped with lenses with a focal length of 75 mm. The cameras are placed at a virtual distance of 0.83 m resulting in a magnification of 0.12 and a digital resolution of 22.9 voxel.mm^{-1}. The resulting particle displacement in the free stream is about 11 voxel.

Particle images are obtained using standard 2-D Gaussian integration. Two sets of images are generated: a set of idealized particle images (Figure 6, left) and another set of noisy particle images (Figure 6, right). The idealized images contain particles with a diffraction spot size of 2 pixels, resulting in a source density (N_s) of 0.16, and a peak intensity of 512 counts. The intensity of the background is zero. The noisy particle images contain particles with a larger diffraction spot size of 2.5 pixels, resulting in a source density (N_s) of 0.25, and a lower nominal peak intensity of 342 counts. The seeding is modelled to consist of TiO_2 particles with a primary crystal size of 55 nm which are known to form agglomerates with a mean size of about 400 nm (Schrijer et al. 2006). Here, we randomly generate particle diameters from a Gaussian distribution with mean of 400 nm and a standard deviation of 100 nm. The distribution is truncated at two standard deviations, to eliminate extremely small and large particles. The peak intensity is modelled to vary with the 4th power of the physical particle diameter (Adrian and Yao 1985), resulting in particle peak intensities range from 21 to 1731 counts. The particle diameter and peak intensity is attributed to a particle once and does not change through time or per camera. Two noise sources are added: shot noise and thermal noise. Shot noise is dependent on the pixel intensity and is implemented so that for every pixel the intensity is a random realisation from a Poisson distribution with mean that is equal to the intensity of the noise-free image. Thermal noise is independent of the intensity and is generated as random realisations from a Poisson distribution with a constant mean across the image. Mean thermal noise is subtracted before further processing.

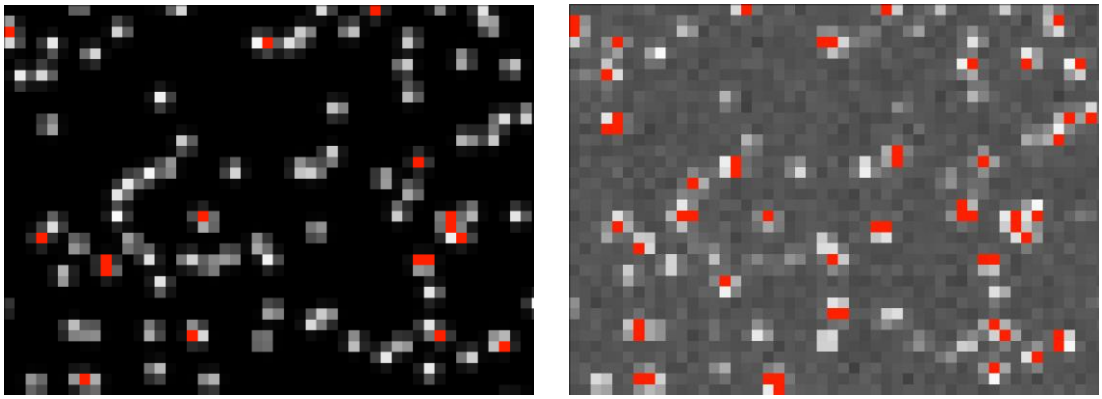

Fig 6. Extracts of a particle image; clean (left) and noisy after subtraction of mean noise intensity (right). In this example, the extracts depict the same region at the same time instance

Despite efforts to make the synthetic experimental data representative of realistic PIV experiments, they remain of unrealistic high quality in the sense that it benefits from an optimal

seeding distribution, optimal camera viewing angles, a perfect corresponding camera calibration, illumination with a uniform intensity, absence of any unwanted light reflections, lens effects and optical distortions due to the non-uniform index of refraction of the flow and the wind tunnel windows. Furthermore, the time-resolved data and multi-pulse data both have been given similar characteristics in the present study. In reality however, time-resolved measurements typically have different characteristics, in particular a lower image quality due to the relatively small light budget of high-speed lasers and the relatively large pixel size of high-speed cameras.

4.4 Tomographic PIV processing

Particle images have been processed using the tomographic PIV algorithms available in LaVision 8.2 software. The settings and procedures used are typical for experimentally obtained particle images, even though the current set of high-quality synthetic images allows processing at a high spatial resolution (i.e. using smaller interrogation windows). Also no multi-frame cross-correlation techniques (e.g. FTEE) have been applied.

The images are calibrated using synthetic images of a structured dot-pattern, followed by volume self-calibration (Wieneke 2008) using the particle images to minimize any inaccuracies in the dot-pattern detection. Reconstructed volumes are obtained using seven iterations of the fast MART algorithm after initialisation, with a uniform value of 1.0. A 3 × 3 × 3 Gaussian smoothing applied after each iteration, excluding the final iteration. The computations are optimized by not updating voxels with intensities below 0.005 counts (Atkinson and Soria 2009).

Vector fields are calculated by cross-correlation of two reconstructed volumes using a multi-grid volume-deformation algorithm. Vector fields from intermediate correlation steps are enhanced for the next iteration by removing spurious vectors, identified by universal outlier detection (Westerweel and Scarano 2005), replacing them using linear interpolation and by Gaussian smoothing of the velocity field. The final three iterations are performed with an interrogation window size of 32 × 32 × 32 voxels at 75% overlap, resulting in a vector spacing of 0.35 mm (8 voxels) and a measurement grid of 171 × 67 × 11 vectors. Each final window contains about 13 particles. No post-processing was applied to the result of the final iteration.

Error estimates are obtained by assessing the difference between the PIV velocity field and the ZDES simulation data interpolated to the PIV grid points. The mean difference represents the bias error and the standard deviation of the difference represents the random error. Error quantities are expressed in voxels displacement, where 1 voxel displacement corresponds to

$0.1U_\infty$. Bias errors were found to be smaller than 0.1 voxel throughout the measurement volume with the exception of a small thin region at the location of the shear layer in the direct vicinity of the step. Figure 7 shows the r.m.s. errors (ε_{RMS}) of the velocity fields obtained with the clean (left) and noisy (right) particle images. Comparison shows that the impact of noise is typically about 0.05 voxel. In most of the domain, the error is < 0.5 voxel. The smallest errors occur in the freestream, where the typical error is < 0.1 voxel, and in the recirculation region. The largest errors can be found in the shear layer and the reattachment region where the largest displacement gradients and smallest spatial and temporal scales occur (see also Figure 5). The error quantities found here are within the typical range of uncertainties of tomographic PIV reported for similar flows (Lynch and Scarano 2014a, 2014b, Blinde et al 2015).

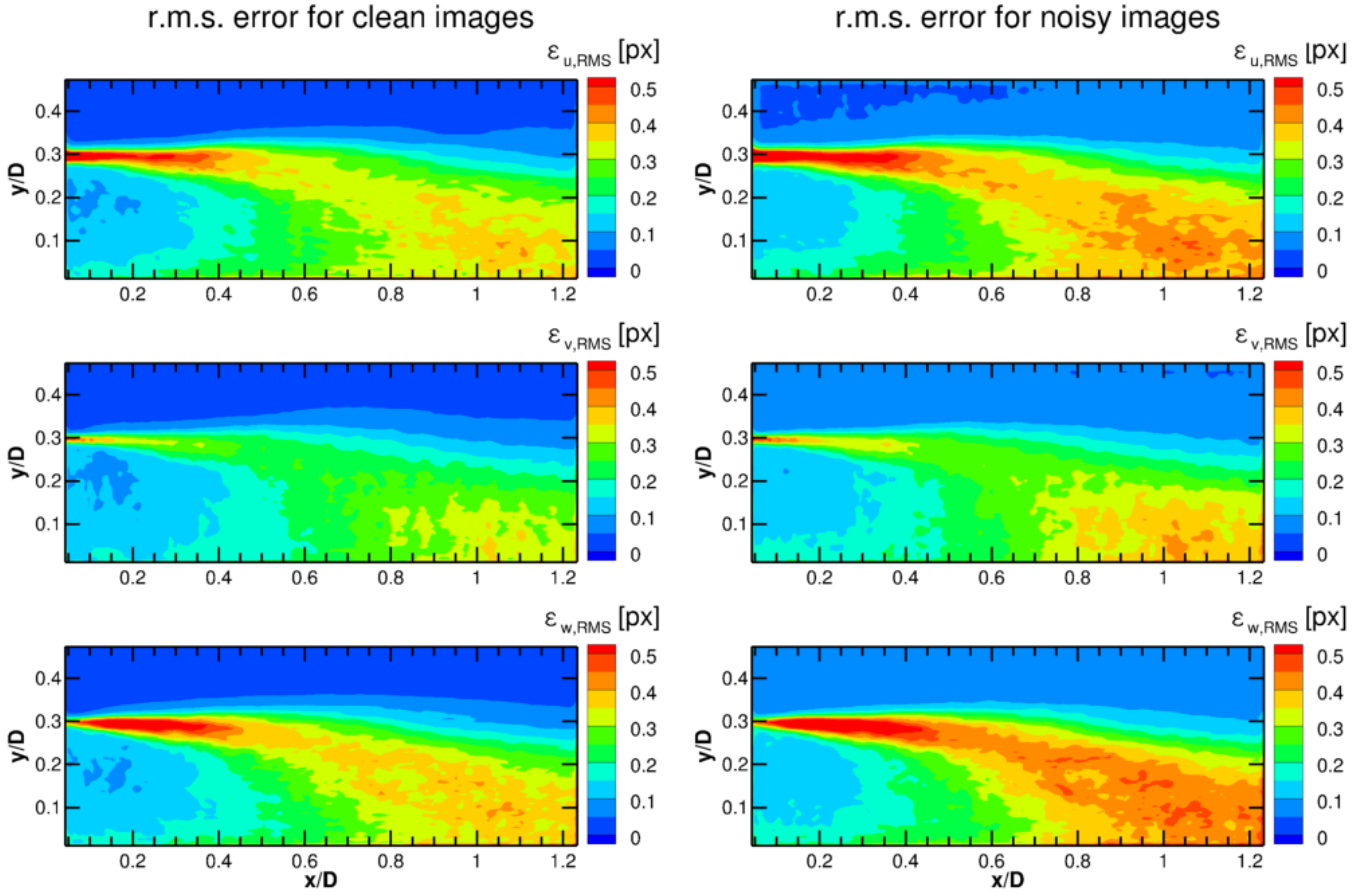

Fig 7. Centre-plane r.m.s error of velocity components, expressed in voxels displacement obtained by PIV processing of the clean (left) and noisy (right) particle images; streamwise (top), wall-normal (middle) and out-of-plane (bottom) direction

4.5 PTV processing ('Shake-The-Box')

For the PTV processing, particle paths are determined using the 'Shake-The-box' algorithm (STB, Schanz et al. 2016). An adapted version of the STB strategy (Novara et al. 2015) has been applied to the multi-pulse data. All cases were processed using DLR in-house codes.

For the initiation phase of the STB PTV processing, the particle distribution in the first four images is determined using Iterative Particle Reconstruction (IPR, Wieneke 2013). Four normal triangulation iterations are performed (m = 4), followed by two triangulation iterations (n = 2) using a reduced set of three cameras. Seven so-called shake iterations are executed after each triangulation (k = 7). The allowed triangulation error is 0.7 px. in the clean case and 1.1 px. in the noisy case. The intensity threshold for particle identification is set to 100 counts and 40 counts, respectively. Tracks are searched in the resulting particle distributions for the four time steps, using a predictor field obtained from a tomographic PIV evaluation. For the time-resolved cases, from the fifth time-step on this predictor is completely replaced by predictions based on already identified particle tracks and the number of triangulation and shake iterations is reduced (m = 3, n = 2, k = 7). Three passes of STB are conducted going forwards and backwards in time to extend any non-identified parts of already detected tracks and to find any previously overlooked tracks. In the end, the algorithm finds over 99% of all available particle tracks for the clean case and around 96 % for the noisy case. A B-spline function is fit through the resulting particle tracks to reduce noise and to obtain Lagrangian velocity and acceleration as derivatives of a continuous function.

Concerning the multi-pulse data, an iterative STB approach strategy is applied, where the sequential application of IPR (m = 4, n = 2, k = 5) and tracking allows to progressively increase the number of reconstructed tracks. The allowed triangulation error is 0.6 px. and 1.1 px. for the clean and noisy case respectively. The intensity threshold for particle identification is set to 20 counts for the clean case, while an adaptive threshold is adopted for the noisy case where the threshold value is progressively reduced for each of the STB iterations. Three STB iterations are applied for the clean case and four for the noisy case. Approximately 99% and 88% of the real four-pulse particle tracks are successfully identified by STB for the clean and noisy case respectively. A 3rd-order B-spline function with a fixed cut-off frequency has been fit through the resulting particle tracks. A more detailed description of the processing method is provided by Novara et al. (2016).

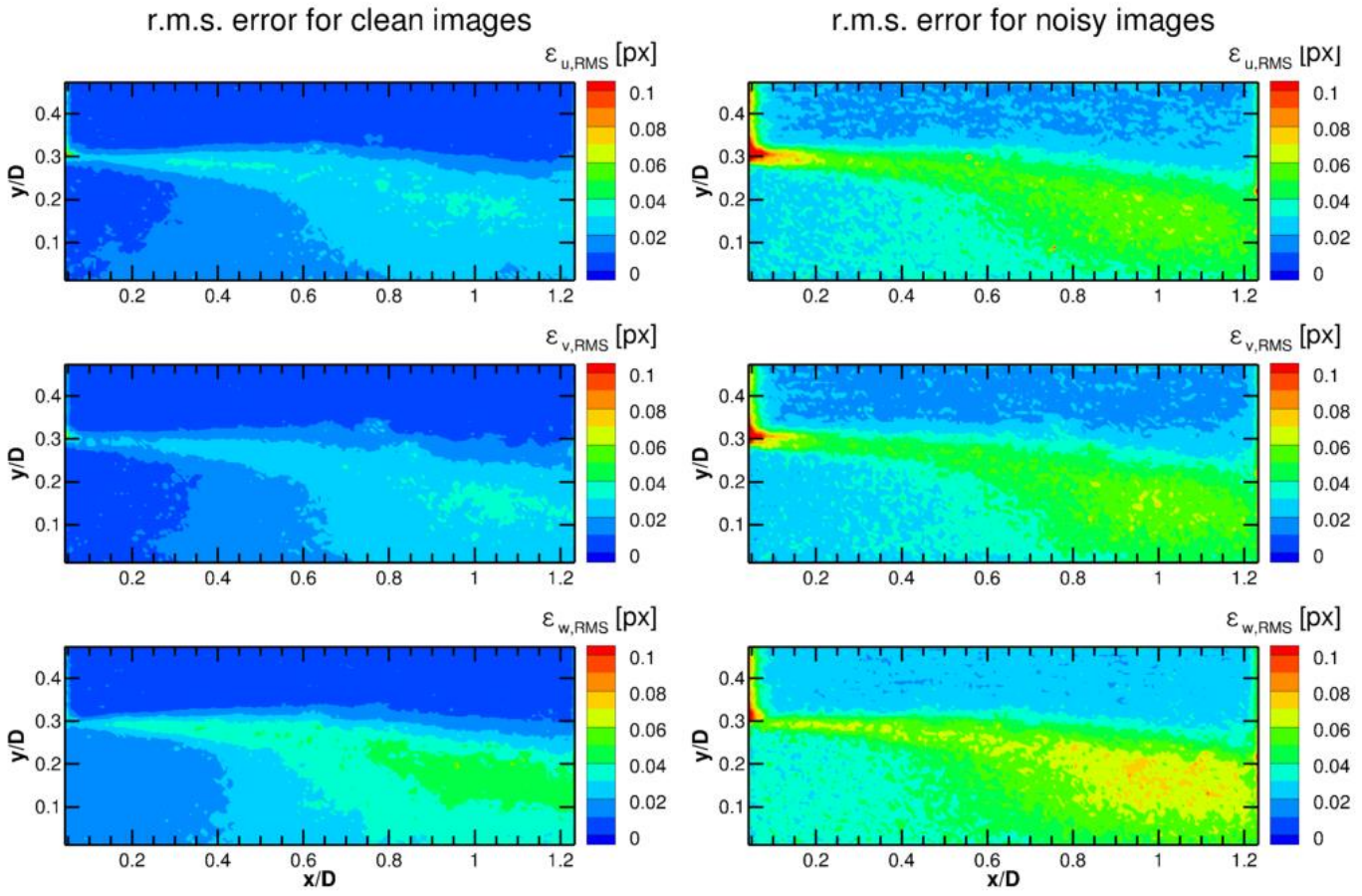

Fig 8: Centre-plane r.m.s. error of velocity components, expressed in voxels displacement obtained by STB processing of the clean (right) and noisy (left) particle images; streamwise (top), wall-normal (middle) and out-of-plane (bottom) direction. Note the difference in scale with respect to Figure 7.

Similar as for the tomo-PIV processing, the velocity error is estimated from the difference between the STB velocity field and the ZDES simulation data interpolated to the particle position and time. Figure 8 shows the r.m.s error (ε_{RMS}) on basis of 5000 time-resolved STB results. Errors in the u- and v-components obtained from the clean particle images (left figures) are of a similar magnitude as the error estimate for the particle integration procedure, suggesting an almost perfect reconstruction. For all other cases, the error typically stays below 0.05 voxel. Larger errors occur at the in- and outflow where not all tracks are immediately identified and the particle tracks can benefit less from the information from adjacent time instances. Similar features as for the PIV results can be observed but error levels are an order of a magnitude smaller (note the different scale). For a large part this can be explained by the absence of the spatial filtering that occurs in the PIV processing, which is especially noticeable in the shear layer. Furthermore, it

should be realized that the comparison is somewhat biased in the sense that the current PIV processing is typical for experimentally obtained particle images and no multi-frame cross-correlation techniques have been applied that would exploit the additional time information available, whereas the application of the STB algorithm has not yet been experimentally demonstrated for the present flow case (i.e. a high-speed transonic flow).

5. Descriptions of applied pressure evaluation techniques

5.1 Flow modelling assumptions

All methods rely on the momentum equation (equation 1) to determine the pressure gradient from the material acceleration, which is computed from the flow kinematic data. To account for compressibility effects, the momentum equation is rewritten to eliminate density as independent variable, under the assumption of inviscid and adiabatic flow (van Oudheusden et al. 2007). The high Reynolds number of the current flow justifies the inviscid flow approximation, while the absence of heat transfer from the model supports the adiabatic assumption.

$$\nabla \ln\left(\frac{p}{p_\infty}\right) = -\frac{1}{RT}\cdot\frac{D\mathbf{u}}{Dt} = -\frac{\gamma M_\infty^2}{V_\infty^2 + \frac{\gamma-1}{2}M_\infty^2(V_\infty^2 - V^2)}\cdot\frac{D\mathbf{u}}{Dt} \tag{4}$$

To provide a boundary condition to the pressure integration, the isentropic pressure ratio (equation 5) is used as Dirichlet boundary condition at the top of the domain or as means of normalisation.

$$\frac{p}{p_\infty} = \left(1 + \frac{\gamma-1}{2}M_\infty^2\left(1 - \frac{V^2}{V_\infty^2}\right)\right)^{\frac{\gamma}{\gamma-1}} \tag{5}$$

Figure 9 investigates the r.m.s. errors introduced by the assumption of adiabatic flow on temperature (top-left) and of isentropic flow on the pressure (top-right). The bottom figures show that the impact of those assumptions on the pressure solution is an order of magnitude smaller than the magnitude of the pressure fluctuations present in the flow (compare Figure 4). For both assessments, the simulation data were first interpolated to the PIV grid points. Material accelerations were calculated by taking the spatial gradient of the reference pressure data. Equation 4 was subsequently solved by prescribing the isentropic pressure ratio at the top boundary and using Neumann boundary conditions at all other boundaries.

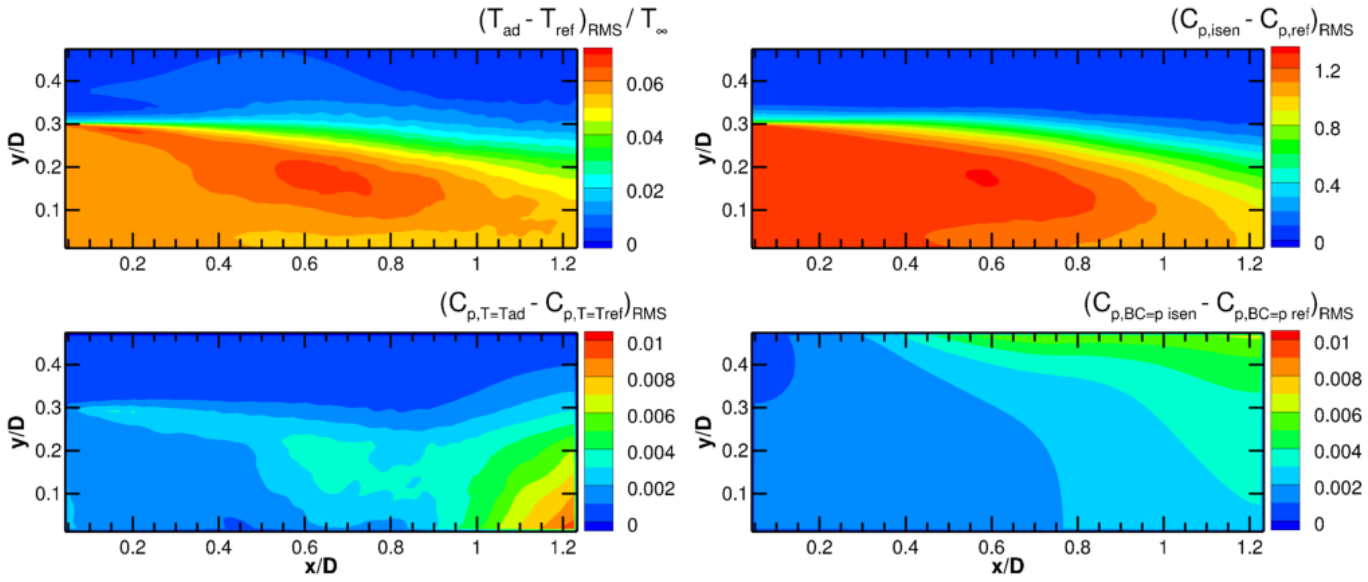

Fig 9. R.m.s. Errors from assuming adiabatic temperature (top-left) and isentropic pressure (top-right) as well as r.ms. impact on pressure solution (bottom figures)

5.2 PIV-based techniques

The following four techniques reconstruct pressure fields from velocity data on a Cartesian grid, as obtained by PIV. These techniques include an Eulerian approach (EUL) and an (iterative) Lagrangian approach (ILAG) which each require at least two subsequent snapshots as input data for determining the material acceleration (multi-snapshot approaches) and the Taylor's hypothesis approach (TH) and the instantaneous vortex-in-cell method (IVIC) which each only require a single velocity snapshot as input data (single-snapshot approaches).

Eulerian approach (EUL)

The material acceleration is evaluated in a stationary reference frame as being composed of temporal and spatial velocity derivatives (see e.g. Baur and Köngeter 1999). In the present implementation these derivatives are evaluated using second-order finite difference discretization except at the boundaries where first-order discretization is used instead. The pressure gradient is integrated by first taking the divergence of equation (4) to obtain a Poisson equation (see e.g. de Kat and van Oudheusden 2012). Neumann boundary conditions are imposed on all sides except for the top surface of the domain, where the pressure as obtained from the isentropic flow relations is prescribed as Dirichlet boundary condition (see equation 5). The problem is discretised using a second-order finite difference scheme and the resulting linear

system is subsequently solved for pressure. The method is implemented using pairs of snapshots with a time separation of 10 μs for both the multi-pulse and the time resolved case.

Iterative least-square pseudo-tracing (ILAG)

Imaginary particles are traced through subsequent velocity fields (see e.g. Liu and Katz 2006). In the present implementation, imaginary particles located at the grid points are integrated forward and backward in time in combination with linear interpolation. The material acceleration is obtained from a first-order least-square fit through the velocity values at the positions of the imaginary particles, disregarding any particle positions outside the domain. For time-resolved PIV, it could also be estimated with the FTEE algorithm (Jeon et al, 2014). The material acceleration is used to obtain a better estimate of the imaginary particle track in a next iteration. The temporal length of each trajectory is 9 time steps for the case of time-resolved input data and 2 time steps for the case of multi-pulse input data. In order to compensate the excluded outward fluid motion at the volume boundary and to prevent corresponding decrement of the dynamic range, the temporal trajectory length is extended toward the opposite side. The spatial integration of the pressure gradient is conducted by solving the Poisson equation formulated as a least-square error cost function on a staggered grid. Neumann boundary conditions are implicitly integrated. A Dirichlet boundary condition with a value of 0 is prescribed in a single grid point. In a next step the solution is offset using the isentropic pressure ratio (see equation 5) sampled over a region selected based on the Frobenius norm of the material acceleration tensor. A detailed description of the present implementation can be found in (Jeon et al. 2015). The method is implemented for both PIV and STB input data. In case of the latter, the temporal length is 2 time steps for both the cases of time-resolved and multi-pulse input.

Taylor's hypothesis approach (TH)

Taylor's hypothesis consists of the assumption that advection due to turbulent circulation is small and that 'frozen' turbulence therefore advects with the flow. Adopting Taylor's hypothesis enables the estimation of the material acceleration from a single velocity snapshot. The choice of convection velocity is crucial for the accuracy of this method and is taken here as the mean streamwise velocity, averaged in z-direction. A detailed description of the implementation of this approach for pressure determination can be found in de Kat and Ganapathisubramani (2013) and Laskari et al. (2016). The subsequent integration of the pressure gradient is performed similarly as for the Eulerian approach described above.

Instantaneous Vortex-in-Cell (IVIC)

In the IVIC method, the material acceleration is approximated from a single-snapshot by application of the vorticity transport equation to the velocity measurement at a single time instant. In summary, the method first evaluates the vorticity temporal derivative by solution of the (inviscid and incompressible) vorticity transport equation. In a next step, the velocity temporal derivative is calculated by solution of a Poisson equation and then used to construct the material acceleration. A more detailed description of the approach can be found in Schneiders et al. (2016). The subsequent integration of the pressure gradient is performed similarly as for the Eulerian approach described above.

5.4 PTV-based techniques

The following four techniques reconstruct pressure fields from acceleration data along particle tracks, as obtained by PTV. These techniques include FlowFit and VIC+ which first interpolate acceleration data to a Cartesian grid and subsequently solve the momentum equation for pressure, as well as FlowFit2 and Voronoi-based integration that directly determine pressure fields from the sparse acceleration data.

FlowFit in combination with FFT integration (FF1)

The acceleration data obtained at the particle positions are interpolated to a Cartesian grid by 'FlowFit'; an iterative optimization approach that generates a quadratic B-splines representation of the acceleration field, using spline coefficients from minimizing a cost function that enforces smoothness and penalizes the curl of acceleration (Gesemann 2015). Integration is performed in Fourier space. A constant pressure offset is added to the solution to yield the absolute pressure field (Huhn et al. 2016).

FlowFit2 (FF2)

Flowfit2 represents the scalar pressure field as 3D cubic B-spline function and estimates its parameters by defining a cost function that is minimized on the basis of a weighted sum of:

- Squared distances between "fitted" and "measured" pressure gradients at all particle positions
- Squared distances between "fitted" and isentropic pressure at the top of the domain
- Squared curvatures of the pressure function as a form of Tikhonov regularization.

The resulting linear least squares problem is solved iteratively. After this reconstruction, the B-spline curve is sampled at the desired points.

Vortex-in-Cell+ (VIC+)

VIC+ reconstructs instantaneous velocity and its material derivative on a regular grid using both the instantaneous velocity and material acceleration evaluated from Lagrangian particle trajectory measurements. The technique follows an iterative procedure that minimizes a cost function and penalizes deviations from the instantaneous velocity and material acceleration measurement. A detailed description of the approach can be found in Schneiders et al. (2015). The subsequent integration of the pressure gradient is performed via a Poisson equation (see Eulerian approach). Pressure gradients are prescribed as Neumann boundary conditions used on all sides of the domain. In a next step, the solution is normalised by setting the mean pressure ratio at the top plane equal to the mean isentropic pressure ratio (see equation (5)). The method is implemented using the STB output for the time-resolved case and the output of an in-house tomographic PTV for the multi-pulse case.

Voronoi-based pressure integration (VOR)

A Lagrangian finite-volume method is utilized to spatially integrate equation (4) to obtain pressure values at the particle positions provided by STB. First, a Lagrangian network is constructed on the particle field (Neeteson and Rival 2015), so that the pressure may be extracted directly in the Lagrangian frame. Next, equation (4) is discretized to the Lagrangian network using a finite-volume method. Neumann boundary conditions are enforced implicitly at all sides excluding the top where a Dirichlet boundary condition is enforced by prescribing the isentropic pressure ratio (see equation 5). The resulting problem is expressed in a system of linear equations, which is solved for pressure.

6. Pressure results

6.1 Pressure from PIV-based techniques

This section presents the results from applying pressure reconstruction techniques to PIV velocity data. Figure 10 and Figure 11 show results and errors for time-resolved and multi-pulse noisy input data, respectively. The results for the clean case are very similar and have therefore been omitted for brevity. Reference pressure from the simulation data is shown in the top-left figure. Each other row corresponds to a different technique. Left figures show sample instantaneous (reconstructed) pressure fields in the centre-plane, with the corresponding instantaneous errors in the centre figures. Right figures show the r.m.s. errors from all available time steps and planes in z-direction. As the error of the reconstructed pressure fields generally increases towards the outer planes, this approach slightly increases the r.m.s. error level with

respect to the error at centre z-plane. The overall comparison is however not affected. The reference pressure is provided for the time instance of EUL and ILAG which is 5 µs later than the depicted time instance for TH and IVIC which reconstruct pressure from a single velocity snapshot.

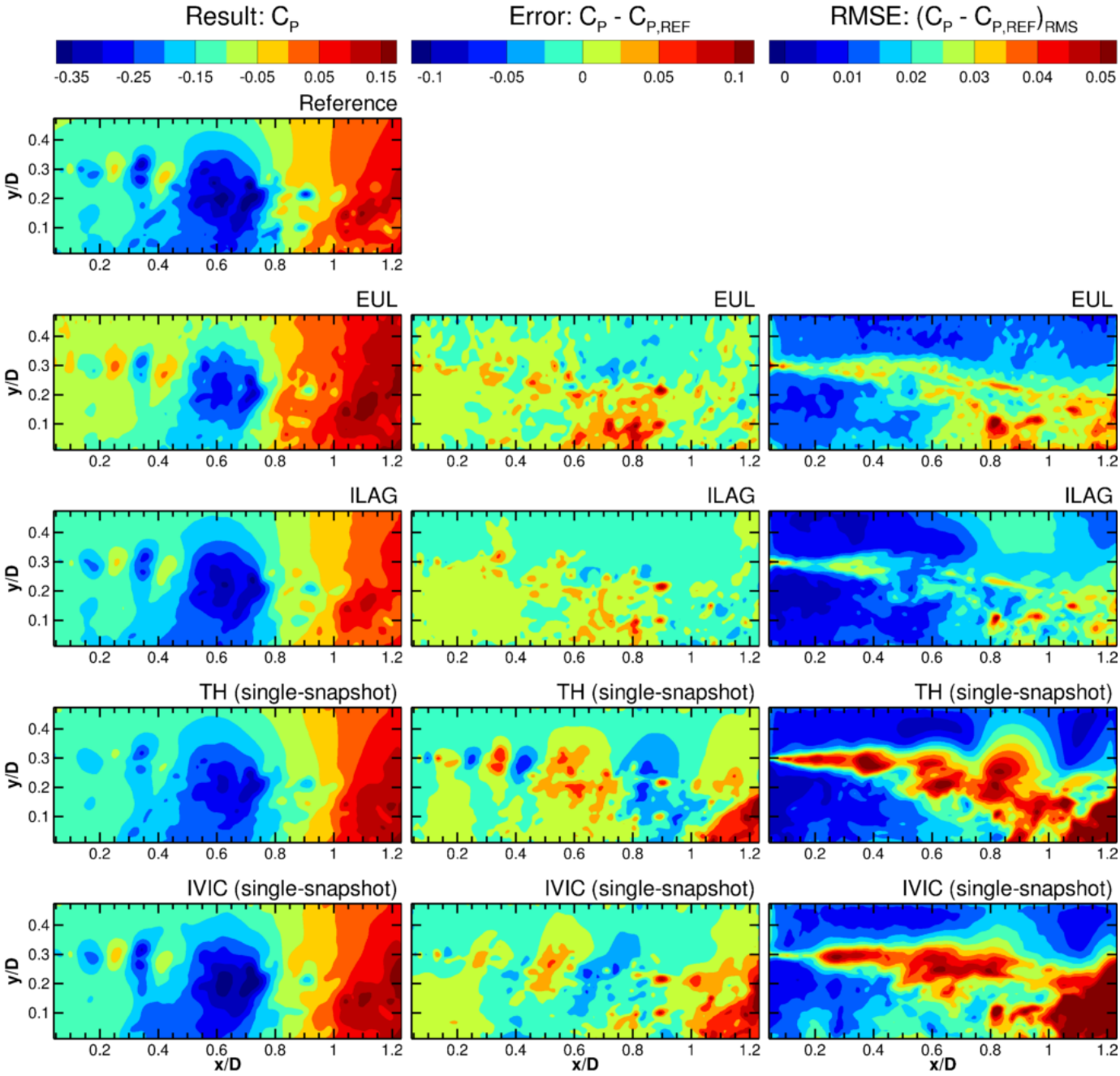

Fig 10. Results and errors from applying PIV-based pressure reconstruction techniques to time-resolved input data. (Reconstructed) instantaneous pressure fields in the centre-plane (left column), instantaneous error in the centre-plane (centre column) and r.m.s. errors for all 11 planes (right column).

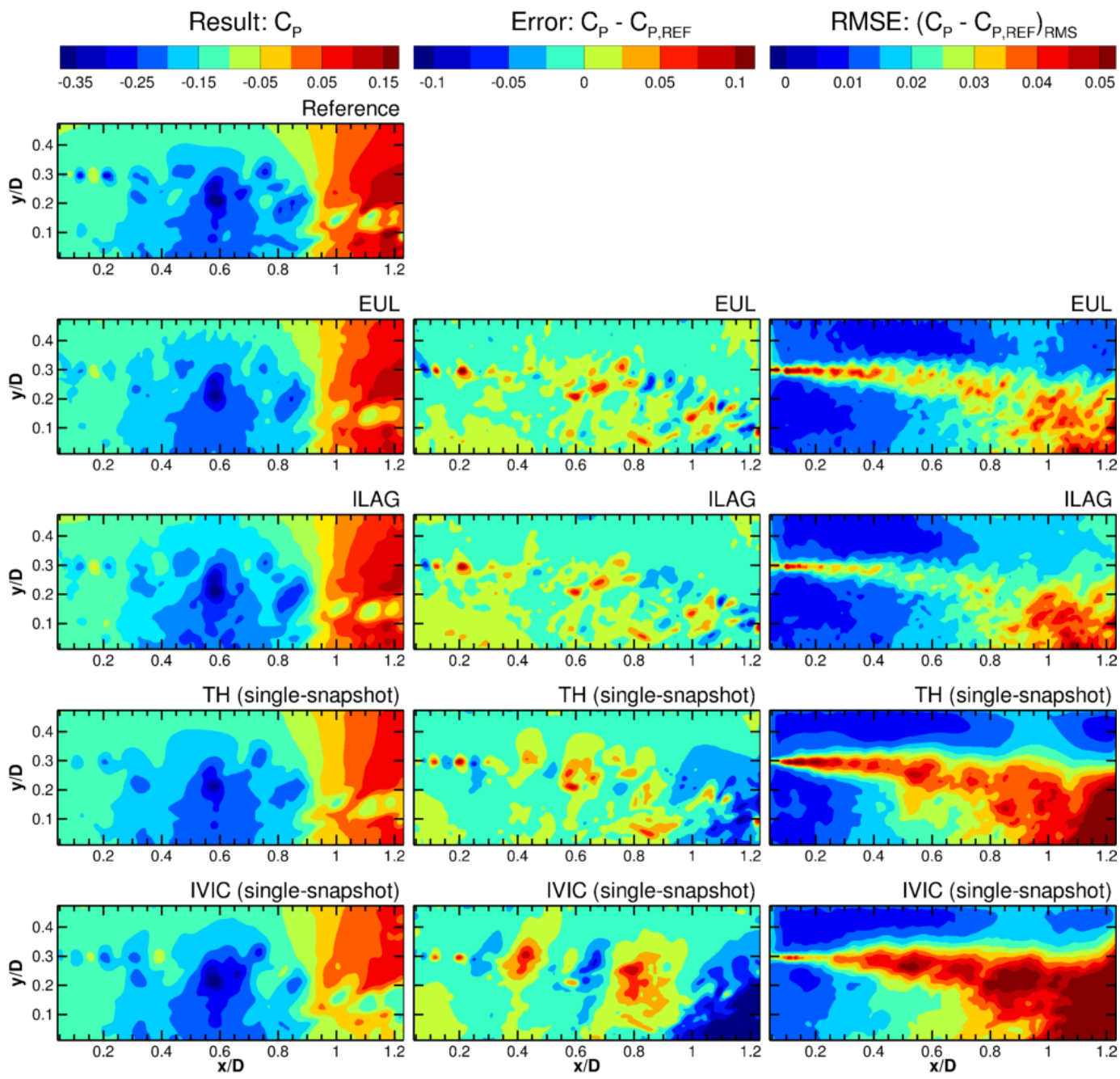

Fig 11. Results and errors from applying PIV-based pressure reconstruction techniques to multi-pulse input data. (Reconstructed) instantaneous pressure fields in the centre-plane (left column), instantaneous error in the centre-plane (centre column) and r.m.s. errors for all 11 planes (right column).

The left figures show that all methods are able to reconstruct the general features of the reference pressure field. The centre and right figures show that all reconstructed pressure fields have the highest error in the shear layer and reattachment region where the smallest temporal and spatial flow scales occur and the precision of the PIV measurement is poorest (see Figure 7). The single-

snapshot approaches (TH and IVIC) can be seen to produce less precise pressure reconstructions than the multi-snapshots approaches (EUL and ILAG); an expected result as EUL and ILAG use more temporal information. Nevertheless, in the light of practical difficulties in obtaining multi-pulse data in high-speed flows, it is encouraging that from this assessment it appears to be quite feasible to reconstruct the main pressure field features from a single velocity snapshot.

Comparing the two multi-snapshot methods shows that Eulerian approach (EUL) leads to less precise pressure reconstructions than ILAG (compare right figures). Investigation of the time-resolved sequence of instantaneous results furthermore shows highly fluctuating error fields for the Eulerian approach (EUL), whereas the error field for ILAG evolves more gradually over time. This is attributed to the better use of temporal information by ILAG, which in the present implementation for the time-resolved fits a 2^{nd}-order polynomial over 9 consecutive velocity fields. The temporal velocity derivative in the current Eulerian approach on the other hand is based on the difference between two velocity fields, a procedure that is known to be sensitive to any velocity measurement noise. For the case of the multi-pulse input data, the difference between the results of both methods is less pronounced as they both only use two velocity snapshots. Here, the slightly lower overall error levels of ILAG may speculatively be attributed to a number of possible causes including the filtering effect of making a polynomial fit, better numerical treatment of regions near the domain boundary and a more suitable time separation between velocity fields. Further comparison shows that the r.m.s. errors for ILAG are relatively high in the top-right of the domain. This is attributed to difference in the boundary condition for pressure integration as contrary to the other methods, as the present implementation of ILAG does not prescribe a pressure ratio at the downstream part of the top boundary.

Comparison of the single-snapshot approaches (TH and IVIC) shows that IVIC better captures the smaller flow structures in the upstream part of the shear layer (for $x/D<0.3$). In the rest of the domain, TH performs better. The performance of TH here is surprisingly good as it was designed to work for convective flows and the underlying assumption of advection of ‘frozen’ turbulent structures is invalid for shear layers and separated flows. The errors of IVIC in the downstream region are likely due to the difficulty in defining a suitable velocity boundary condition in this region, which is inherent to the method and a known sensitive aspect of its implementation.

6.2 Pressure from PTV-based techniques

This section presents the results from applying pressure reconstruction techniques to STB acceleration data. Figure 12 and Figure 13 show results and errors for time-resolved and multi-pulse noisy input data, respectively. Note that the scaling of the instantaneous error (centre figures) has been adapted with respect to section 6.1 to better visualize the error distribution. The scaling of r.m.s. error fields (right figures) remains unchanged to facilitate direct comparison with the PIV-based techniques.

The left figures show that all PTV-based techniques are able to reconstruct the general features of the reference pressure field and that moreover most methods provide similar results, especially for the time-resolved data (Fig.12). Errors for the time-resolved input data are lower than for the multi-pulse input data, which is attributed to lower accuracy of the particle tracks in the latter case. Comparison of results of the different techniques shows that the results for FlowFit1 and FlowFit2 are very similar and VIC+ yields the most accurate pressure reconstruction. Errors for the Voronoi-based integration approach (VOR) are significantly higher than for the other PTV-based methods.

Comparison with the PIV-based approaches shows significantly lower error levels for the PTV-based approaches. This is in line with the lower velocity errors from PTV processing compared to PIV processing for the present test case (compare Figure 7 and Figure 8). Another indication that the lower errors are driven by the better input data is that the ILAG approach performs much better when using PTV data than when using PIV data because the acceleration is directly estimated from the particle motion.

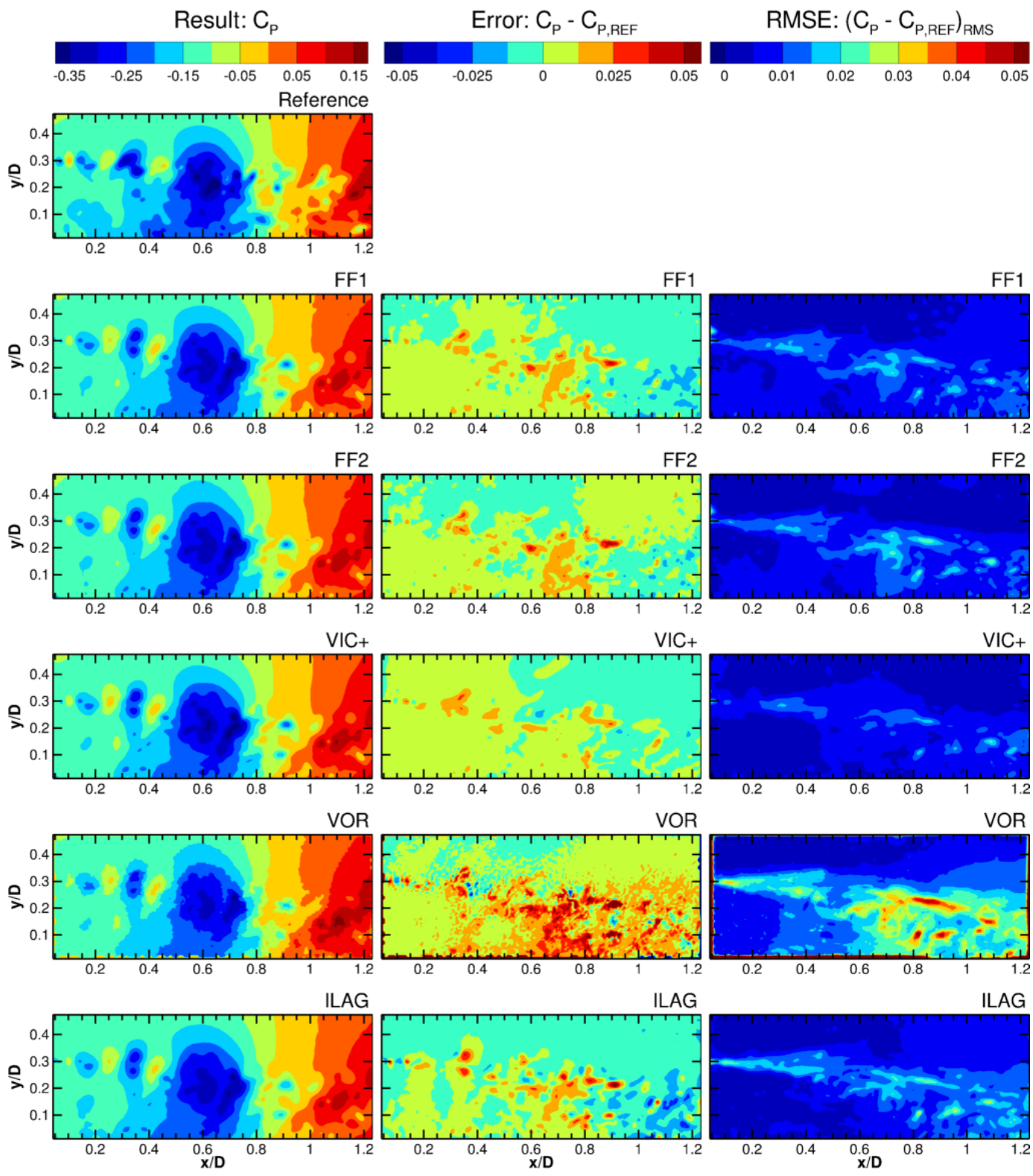

Fig 12. Results and errors from applying STB-based pressure reconstruction techniques to time-resolved input data. (Reconstructed) instantaneous pressure fields in the centre-plane (left column), instantaneous error in the centre-plane (centre column) and r.m.s. errors for all 11 z-planes (right column); r.m.s. error for Voronoi-based integration considers 5 z-planes only.

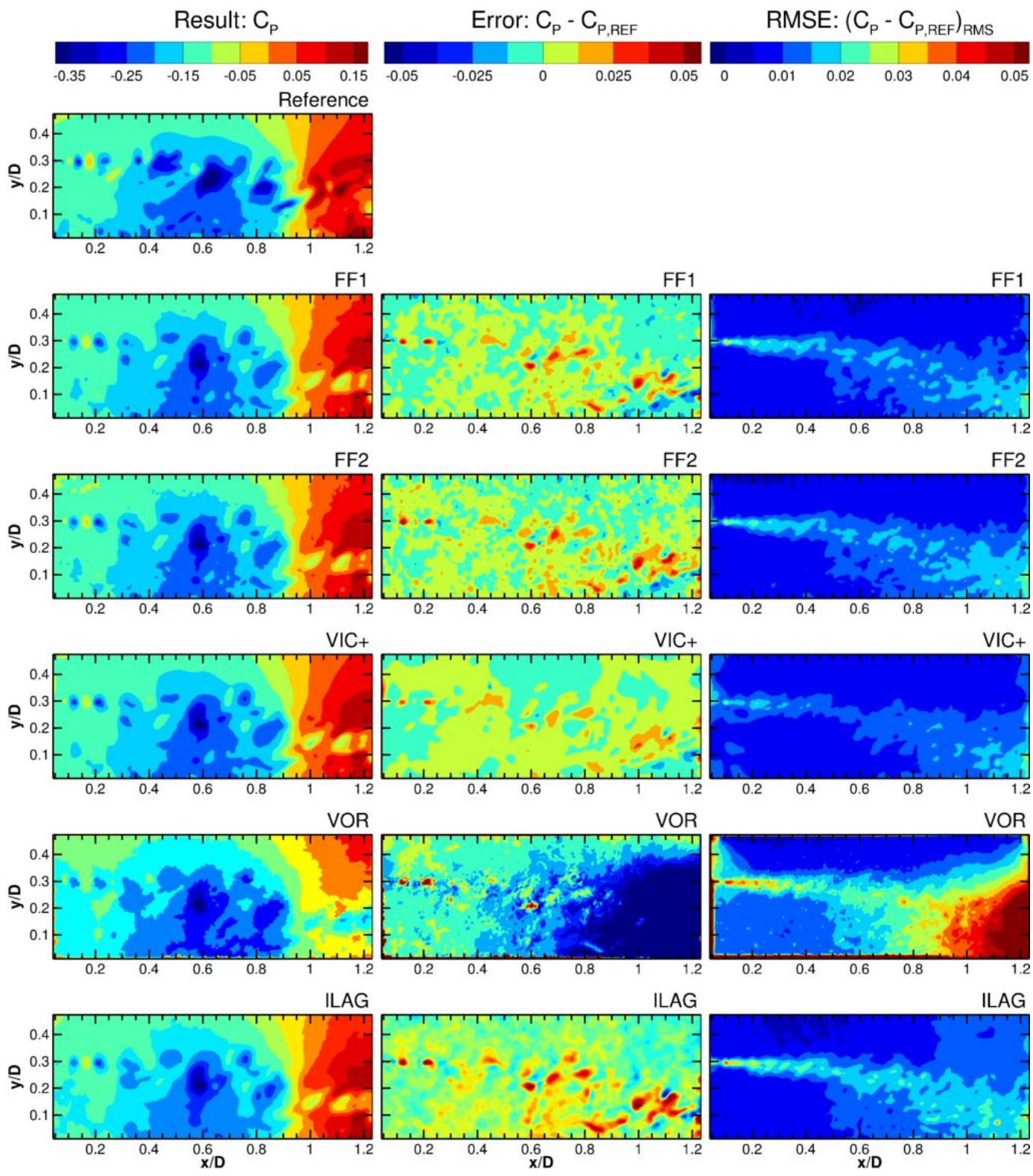

Fig 13. Results and errors from applying STB-based pressure reconstruction techniques to multi-pulse input data. (Reconstructed) instantaneous pressure fields in the centre-plane (left column), instantaneous error in the centre-plane (centre column) and r.m.s. errors for all 11 z-planes (right column); r.m.s. error for Voronoi-based integration considers 5 z-planes only.

6.3 Overview of results

To further quantify and compare the performance of different methods, the global errors (ε) is obtained by taking the r.m.s. error for all gridpoints (N_p) at all time instances (N_t):

$$\varepsilon \approx \sqrt{\frac{1}{N_t N_p}\sum_{i=1}^{N_t}\sum_{j=1}^{N_p}\left(\left(C_p\right)_{i,j}-\left(C_{p,ref}\right)_{i,j}\right)^2} \tag{6}$$

Table 3 and Table 4 shows the resulting errors for the clean (left columns) and noisy (right columns) cases for the time-resolved and multi-pulse input data, respectively. The methods have been ordered in terms of increasing error. Errors for the noisy case (right columns) can be seen to be slightly higher than for the clean case (left columns). Where this is not the case, this is attributed to a lack of statistical convergence. The results for the clean and noisy case follow a similar trend which suggests that none of the methods is critically sensitive to the amount of noise added in this test case. Note that Table 4 also includes the result of the VIC+ method using tomo-PTV input data. The error when using this input data remains below the PIV results, but is slightly higher than when STB is used for particle tracking. This shows that less advanced particle tracking methods than STB can still yield acceptable pressure reconstruction quality. The comparison of different particle tracking techniques was left outside the scope of this assessment.

Table 3. Global errors for time-resolved input data. Values are based on 171 × 67 × 11 data points with the exception of VOR which is based on 165 × 61 × 6 data points

Pressure reconstruction	**Source of input data**	**Global error [× 10^{-2}]**	
		Clean	**Noisy**
VIC+	STB	0.68	0.63
FF1	STB	0.72	0.78
FF2	STB	0.72	0.78
ILAG	STB	0.90	0.91
VOR	STB	1.70	1.66
ILAG	PIV (9 snapshots)	1.43	1.69
EUL	PIV (2 snapshots)	1.52	2.09
TH	PIV (1 snapshot)	2.23	2.54
IVIC	PIV (1 snapshot)	3.44	2.99

Table 4. Global errors for multi-pulse input data. Values are based on 171 × 67 × 11 data points with the exception of VOR which is based on 165 × 61 × 6 data points.

Pressure reconstruction	Source of input data	Global error [× 10^{-2}]	
		Clean	Noisy
VIC+	STB	0.70	1.02
FF1	STB	0.81	1.07
FF2	STB	0.86	1.10
ILAG	STB	0.99	1.23
VIC+	Tomo-PTV	0.95	1.36
ILAG	PIV	1.67	2.01
EUL	PIV	1.80	2.11
VOR	STB	3.57	2.35
TH	PIV (1 snapshot)	2.66	2.78
IVIC	PIV (1 snapshot)	3.34	3.39

7. Conclusions

A test case for different PIV-based and PTV-based pressure evaluation techniques has been developed by constructing a simulated experiment from ZDES simulation data. Important experimental error sources are replicated by simulating the entire measurement chain. To enable an assessment of the impact of measurement noise, the test case includes both cases with and without added artificial noise. The test case includes multi-pulse data (4 particle images; 2 velocity snapshots), which is representative of the acceleration measurement procedure available in high-speed flows, as well as longer series of continuous time-resolved data which are typically achievable only for low-speed flows. Both tomographic PIV algorithms and the STB algorithm have been applied to enable the testing of both PIV- and PTV-based pressure determination procedures.

A variety of state-of-the-art pressure determination techniques has been applied to a single test case consisting of a transonic flow over an axisymmetric step. The working principles as well as the implementation of these techniques have been described. Using the test case, the techniques have been assessed in terms of their capability to reconstruct the reference pressure field as well as the impact of noise in the input data and the benefit of using time-resolved data. This led to the following main conclusions:

1. A range of suitable methods exists that can reconstruct instantaneous pressure fields from a variety of PIV/ PTV input data. The main features of the pressure fields can be

reconstructed from a single PIV velocity snapshot while highly accurate pressure reconstructions can be obtained by using PTV approaches in combination with more advanced techniques.

2. For the present input data, the PTV-based techniques produce more accurate pressure reconstructions than the PIV-based approaches. This difference in performance is attributed to a combination of higher spatial resolution of the input data and better use of time information in the data sets. It should be realized however that the comparison is biased in the sense that the PIV processing used here is typical for experimentally obtained particle images and no multi-frame cross-correlation techniques have been applied whereas the application of the STB algorithm has not yet been experimentally demonstrated for high-speed flow conditions.
3. The use of longer series of time-resolved input data allows more accurate reconstructions of the reference pressure field. Nevertheless, in light of practical difficulties in obtaining multi-pulse data for high-speed flows, it is encouraging that it appears to be possible to reconstruct the main features of the pressure field already from a single velocity field.
4. Noise in the input data typically reduces the accuracy of the reconstructed pressure fields, but none of the methods proved to be critically sensitive to the amount of noise that was added in the present test case.

Given these conclusions on the availability and performance of pressure reconstruction algorithms and their dependence on suitable experimental data, future advances are best attained through demonstration and further development of experimental capabilities.

9. Acknowledgements

This work is supported by the European FP-7 project “NIOPLEX”, grant agreement 605151.

10. References

Adrian RJ, Yao C-S (1985) Pulsed laser technique application to liquid and gaseous flows and the scattering power of seed materials. Appl Opt 24:44. doi: 10.1364/ AO.24.000044

Atkinson C, Soria J (2009) An efficient simultaneous reconstruction technique for tomographic particle image velocimetry. Exp Fluids 47:553–568. doi: 10.1007/ s00348-009-0728-0

Baur T, Köngeter J (1999) PIV with high temporal resolution for the determination of local pressure reductions from coherent turbulence phenomena. 3rd Int. Work. Part. image Velocim., Santa Barbara, CA

Blinde PL, Lynch KP, van Oudheusden BW, Schneiders JFG, Schrijer FFJ (2014) Assessment of instantaneous pressure determination in a transonic base flow based on four-pulse tomographic PIV. 17th Int. Symp. Appl. Laser Tech. to Fluid Mech.

Blinde PL, Lynch KP, van Oudheusden BW, Schrijer FFJ (2015) Determination of instantaneous pressure in a transonic base flow using four-pulse tomographic PIV. 11th Int. Symp. Part. Image Velocim. - PIV15

de Kat R, Ganapathisubramani B (2013) Pressure from particle image velocimetry for convective flows: a Taylor's hypothesis approach. Meas Sci Technol 24:024002. doi: 10.1088/ 0957-0233/ 24/ 2/ 024002

de Kat R, van Oudheusden BW (2012) Instantaneous planar pressure determination from PIV in turbulent flow. Exp Fluids 52:1089–1106. doi: 10.1007/ s00348-011-1237-5

Deck S (2005) Zonal-Detached-Eddy Simulation of the Flow Around a High-Lift Configuration. AIAA J 43:2372–2384. doi: 10.2514/ 1.16810

Deck S (2012) Recent improvements in the Zonal Detached Eddy Simulation (ZDES) formulation. Theor Comput Fluid Dyn 26:523–550. doi: 10.1007/ s00162-011-0240-z

Deck S, Thorigny P (2007) Unsteadiness of an axisymmetric separating-reattaching flow: Numerical investigation. Phys Fluids 19:065103. doi: 10.1063/ 1.2734996

Elsinga GE, Scarano F, Wieneke B, van Oudheusden BW (2006) Tomographic particle image velocimetry. Exp Fluids 41:933–947. doi: 10.1007/ s00348-006-0212-z

Gesemann S (2015) From Particle Tracks to Velocity and Acceleration Fields Using B-Splines and Penalties. arXiv: 1510.09034v1

Huhn F, Schanz D, Gesemann S, Schröder A (2016) FFT integration of instantaneous 3D pressure gradient fields measured by Lagrangian particle tracking in turbulent flows (submitted to Exp Fluids)

Jeon YJ, Chatellier L, David L (2014) Fluid trajectory evaluation based on an ensemble-averaged cross-correlation in time-resolved PIV. Exp Fluids 55:1766. doi: 10.1007/ s00348-014-1766-9

Jeon YJ, Chatellier L, Beaudoin A, David L (2015) Least-square reconstruction of instantaneous pressure field around a body based on a directly acquired material acceleration in time-resolved PIV, 11th Int. Symp. Part. Image Velocim. - PIV15

Laskari A, de Kat R, Ganapathisubramani B (2016) Full-field pressure from snapshot and time-resolved volumetric PIV. Exp. Fluids 57:1–14. doi: 10.1007/ s00348-016-2129-5

Liu X, Katz J (2006) Instantaneous pressure and material acceleration measurements using a four-exposure PIV system. Exp Fluids 41:227–240. doi: 10.1007/ s00348-006-0152-7

Lynch KP, Scarano F (2014a) Material acceleration estimation by four-pulse tomo-PIV. Meas Sci Technol 25:084005. doi: 10.1088/ 0957-0233/ 25/ 8/ 084005

Lynch KP, Scarano F (2014b) Experimental determination of tomographic PIV accuracy by a 12-camera system. Meas Sci Technol 25:084003. doi: 10.1088/ 0957-0233/ 25/ 8/ 084003

Malik N, Dracos T, Papantoniou D (1993) Particle tracking velocimetry in three-dimensional flows. Exp Fluids 15-15:279–294. doi: 10.1007/ BF00223406

Neeteson NJ, Rival DE (2015) Pressure-field extraction on unstructured flow data using a Voronoi tessellation-based networking algorithm: a proof-of-principle study. Exp Fluids. 56:44 doi: 10.1007/ s00348-015-1911-0

Novara M, Scarano F (2013) A particle-tracking approach for accurate material derivative measurements with tomographic PIV. Exp Fluids 54:1584. doi: 10.1007/ s00348-013-1584-5

Novara M, Schanz D, Kähler CJ, Schröder A (2015) Shake-The-Box for multi-pulse tomographic systems : towards high seeding density particle tracking in high speed flows. 11th Int. Symp. Part. Image Velocim.

Novara M, Schanz D, Lynch K and Schroeder A (2016) Lagrangian 3D particle tracking for multi-pulse systems: performance assessment and application of Shake-The-Box, 18th Lisbon Int Symp (present conference)

Ragni D, Schrijer F, van Oudheusden BW, Scarano F (2010) Particle tracer response across shocks measured by PIV. Exp Fluids 50:53–64. doi: 10.1007/ s00348-010-0892-2

Scarano F (2013) Tomographic PIV: principles and practice. Meas Sci Technol 24:012001. doi: 10.1088/ 0957-0233/ 24/ 1/ 012001

Schanz D, Gesemann S, Schröder A (2016) Shake-The-Box: Lagrangian particle tracking at high particle image densities. Exp Fluids 57:70. doi: 10.1007/ s00348-016-2157-1

Schneiders JFG, Pröbsting S, Dwight RP, van Oudheusden BW, & Scarano F. (2016). Pressure estimation from single-snapshot tomographic PIV in a turbulent boundary layer. Experiments in Fluids, 57(4), 53. doi:10.1007/ s00348-016-2133-9

Schneiders JFG, Azijli I, Scarano F, Dwight RP (2015) Pouring time into space. 11th Int. Symp. Part. Image Velocim. - PIV15, Santa Barbara, CA

Schrijer FFJ, Scarano F, van Oudheusden BW (2006) Application of PIV in a Mach 7 double-ramp flow. Exp Fluids 41:353–363. doi: 10.1007/ s00348-006-0140-y

Souverein LJ, van Oudheusden BW, Scarano F, Dupont P (2009) Application of a dual-plane particle image velocimetry (dual-PIV) technique for the unsteadiness characterization of a

shock wave turbulent boundary layer interaction. Meas Sci Technol 20:074003. doi: 10.1088/ 0957-0233/ 20/ 7/ 074003

Tronchin T, David L, Farcy A, (2015) Evaluation of pressure field and fluid forces for 3D flow around flapping wing. Experiments in Fluids, Vol. 56:1, http:/ / dx.doi.org/ 10.1007/ s00348-014-1870-x

van Oudheusden BW (2013) PIV-based pressure measurement. Meas Sci Technol 24:032001. doi: 10.1088/ 0957-0233/ 24/ 3/ 032001

van Oudheusden BW, Scarano F, Roosenboom EWM, Casimeri EWF, Souverein LJ (2007) Evaluation of integral forces and pressure fields from planar velocimetry data for incompressible and compressible flows. Exp Fluids 43:153–162. doi: 10.1007/ s00348-007-0261-y

Weiss P-E, Deck S, Robinet J-C, Sagaut P (2009) On the dynamics of axisymmetric turbulent separating/ reattaching flows. Phys Fluids 21:075103. doi: 10.1063/ 1.3177352

Weiss P-E, Deck S (2011) Control of the antisymmetric mode (m=1) for high Reynolds axisymmetric turbulent separating/ reattaching flows. Phys Fluids 23:095102. doi: 10.1063/ 1.3614481

Westerweel J, Scarano F (2005) Universal outlier detection for PIV data. Exp Fluids 39:1096–1100. doi: 10.1007/ s00348-005-0016-6

Wieneke B (2008) Volume self-calibration for 3D particle image velocimetry. Exp Fluids 45:549–556. doi: 10.1007/ s00348-008-0521-5

Wieneke B (2013) Iterative reconstruction of volumetric particle distribution. Meas Sci Technol 24:024008. doi: 10.1088/ 0957-0233/ 24/ 2/ 024008